Received: 19 December 2023 | Accepted: 29 May 2024

DOI: 10.1002/maco.202314245

ARTICLE

Materials and Corrosion

Quantifying intergranular corrosion susceptibility in AA2098-T351 weldments through friction stir welding

Mariana X. Milagre[1] | **Uyime Donatus**[1] | **Naga V. Mogili**[2] | **Caruline S. C. Machado**[1] | **João Victor. S. Araujo**[1] | **Rejane Maria P. Silva**[1] | **Renato A. Antunes**[3] | **Sajid Farooq**[4] | **Isolda Costa**[1]

[1]Instituto de Pesquisas Energéticas e Nucleares—IPEN/CNEN, São Paulo, Brazil

[2]Laboratório Nacional de Nanotecnologia—LNNano/CNPEN, Campinas, Brazil

[3]Universidade Federal do ABC, Centro de Engenharia, Modelagem e Ciências Sociais Aplicadas, Santo André, Brazil

[4]College of Mathematical Medicine, Zhejiang Normal University, Jinhua, People's Republic of China

Correspondence
Sajid Farooq, College of Mathematical Medicine, Zhejiang Normal University, Jinhua, 321004, People's Republic of China.
Email: sajid@zjnu.edu.cn

Funding information
FAPESP:2013/13235-6; FAPES:Proc.2017/03095-3; Proc. 2018/06880-6; CAPES: 99999.000332/2016-00; CAPES:99999.000400/2016-05; CAPES (Capes/Cofecub No 806-14)

Abstract

In this study, the intergranular corrosion (IGC) susceptibility of AA2098-T351 welds, fabricated through friction stir welding (FSW), was systematically evaluated. The evaluation employed American Society for Testing and Materials (ASTM) G110-92 practice and electrochemical impedance measurements, with comparative analyses against unwelded alloys (BS). The key findings depicted that FSW-induced microstructure changes significantly influenced IGC susceptibility across different zones. Zones affected by FSW presented distinct susceptibilities compared with the base metal (BM). The ASTM G110-92 test effectively differentiated the heat-affected zone (HAZ) into segments with changing corrosion resistances based on welding temperature gradients. Cross-sectional analyses using scanning electron microscopy (SEM) techniques correlated corrosion characteristics with microstructural features identified by transmission electron microscopy (TEM). Overall, FSW-induced microstructural alterations emerged as a predominant factor influencing the varying susceptibilities of different zones to IGC, and electrochemical impedance measurements (EIS) validated the findings from ASTM G110-92 practice.

KEYWORDS

aluminum-lithium alloys, base metal, friction stir welding, intergranular corrosion

1 | INTRODUCTION

In contemporary transportation applications, notably in the aerospace and automotive sectors, the demand for lighter materials and structures is driven by the imperative to reduce fuel consumption and emissions.[1,2] The studies reveal that a 10% weight reduction can result in a remarkable 6%–8% increase in fuel economy for automobiles.[3] The assembly of lightweight structural components is thus critical across diverse industries, and welding or joining is a preferred method due to its efficiency and cost-effectiveness in design. Weldability is recognized as a central criterion in qualifying materials for exclusive use, influencing the feasibility and efficiency of assembly processes in weight-sensitive applications.

The friction stir welding (FSW) process, invented in 1991, serves as a novel technique for welding materials that are difficult to weld through conventional methods.[4] A distinctive feature of FSW is its ability to achieve welding without the need for melting. Heat generation is assisted by the rotational and traverse motions of a tool in direct contact with the materials to be welded. This dynamic tool action induces friction, generating sufficient heat to soften and weld the materials in question. Notably, FSW demonstrates particular efficacy in the welding of aluminum (Al) alloys, making it a preferred method in the

aerospace industry. This technique's nonmelting nature and its capability to maintain material integrity during welding contribute to its widespread utilization in critical applications.[5,6]

Despite the commendable mechanical features generated by the FSW process, it induces changes in the microstructural characteristics of the welded material. The FSW process exposes the weld joint and its proximal regions to distinct thermal cycles, thus depicting zones categorized based on the heating and mechanical effects on the alloy microstructure.[7] The stir zone (SZ), located where a confluence of the welded materials transpires, experiences the highest temperatures during the FSW process, causing recrystallization and phase dissolution. In the thermomechanically affected zone (TMAZ), the rotational dynamics of the pin and the material flow constraints imposed by the tool shoulder, coupled with elevated temperatures, result in grain deformation, phase dissolution, and coarsening. The heat-affected zone (HAZ), while not experiencing temperatures sufficient to induce alterations in grain shape, manifests dissolution and phase coarsening.[8–13] The various microstructures within the welded alloys, interacting in the aforementioned zones, exert a profound influence on their reactivity in aggressive environments. Specifically, one of the predominant corrosion mechanisms in Al alloys is intergranular corrosion (IGC), leading to grain detachment and consequent loss of mechanical behavior. It is noteworthy that the IGC resistance of Al–Cu–Li alloys remains a relatively understudied aspect within the current scientific literature.[11–15]

The American Society for Testing and Materials (ASTM)-G110 standard practice stands as a basic methodology for evaluating the susceptibility of Al alloys to IGC in acid environments.[16–19] According to study,[20,21] the occurrence of IGC demands specific conditions: (1) the presence of a solute-depleted zone along grain boundaries (GB) in the alloy; (2) the corrosive medium containing anions capable of disrupting passivity at vulnerable regions; (3) the breakdown potential of the depleted zone being lower than that of Al; and (4) the corrosion potential of the alloy exceeding the breakdown potential of the depleted zone while being below the breakdown potential of the grain bodies. Liang et al.[22] reported that IGC in Al–Cu–Li alloys is generated by the preferential dissolution of the T1 (Al_2CuLi) phase, integrated with a precipitate-free zone (PFZ). Ambat et al.[23] examined a pH-dependent susceptibility to IGC, with increase corrosion rates being exhibited in strongly acidic/alkaline chloride solutions. Additionally, extensive pitting and localized attacks were detected in neutral pH solutions. Kumai et al.[24] corroborated the phenomenon, attributing IGC in Al–Cu–Li alloys to copper-depleted zones. The plethora of literature on the IGC corrosion susceptibility of Al–Cu–Li alloys is rare and even scarcer when attributed to the FSW process.[25,26]

This study delves into the IGC susceptibility of AA2098-T351 welds generated through FSW, utlizing the ASTM G110 standard for evaluation. The findings are juxtaposed with those of the base metal and correlated with the microstructural alterations induced by the welding process. Furthermore, electrochemical impedance measurements (EIS) established the findings derived from ASTM G110-92 practice, reinforcing the in-depth and cohesive assessment of IGC susceptibility in AA2098-T351 welds.

2 | METHODS AND MATERIALS

This study utilized 3 mm thick plates of AA2098-T351 Al–Cu–Li alloy. The composition of the alloy comprises 3.4 wt.% Cu, 1 wt.% Li, 0.3 wt.% Mg, 0.3 wt.% Ag, 0.4 wt.% Zr, 0.04 wt.% Fe, 0.05 wt.% Si, 0.02 wt.% Zn, and 0.003 wt.% Mn. The material has been solution heat treated and stress relieved by stretching (temper T351).

2.1 | FSW process

The FSW process was conducted with a rotation speed of 700 rpm, a traverse speed of 300 mm/min, and a variable load within the range of 8–15 kN. Employing a H13 steel tool featuring a 16 mm diameter shoulder and an adjustable pin of 3.2 mm length, aligned with the plate thickness, the welding process was performed. Thermocouples were technically positioned beneath the plates at distances of 6, 9, and 12 mm from the joint center to capture the thermal profile. Temperature simulations, assessed by the finite element method (COMSOL multiphysics v5.2 software), incorporated key welding phenomena such as conduction and radiation heat transfer. The welding model constructed 86,009 elements, with thermocouple-derived measurements serving as input data for calibrating the thermomechanical model. For an in-depth understanding of the thermal simulation, additional details are available in our prior work.[27]

2.2 | Microstructural characterization

The cross-section of the Al alloy samples was prepared for tests by mechanical grinding with silica carbide abrasives (#320, #550, #800, #1200, #4000) followed by polishing with diamond suspensions of 3 and 1 μm. An etching solution composed of 25% HNO_3 and 3% HF

in deionized H_2O was used to reveal microstructural features. Electrolytic etching was performed in a solution composed of 20 vol.% of nitric acid in methanol at 25 V and at −30°C before acquisition of transmission electron microscopy (TEM) images of the near-surface regions of the samples. TEM samples were prepared using TenuPol equipment. Imaging data were obtained using a JEOL 2100 microscope. Optical and scanning electron microscopy (SEM) images were acquired using a Leica model DMLM microscope and a Hitachi TM 3000 microscope with an incident beam of 15 keV, respectively, from the cross-section of the near-surface regions of the samples.

2.3 | Surface preparation techniques

For the IGC-Test and for the EIS analysis, sample surfaces experienced the following preparation steps: (1) immersion for 1 min in an etching solution comprising 945 mL of deionized water, 50 mL of nitric acid (70%), and 5 mL of hydrofluoric acid; (2) rinsing in deionized water; (3) immersion for 1 min in concentrated nitric acid (70%); (4) rinsing in deionized water; and (5) drying under a hot air stream.

2.4 | IGC susceptibility

Following the surface preparation, the specimens were immersed for 6 h in the solution used for the IGC susceptibility test according to the ASTM G110-92 practice. This solution comprised of 57 g of NaCl and 10 mL of H_2O_2 in 1 L of deionized water. The volume/area ratio of the test solution used was 5 $mL.cm^{-2}$.

2.5 | Electrochemical impedance spectroscopy analysis

EIS tests were performed using an AUTOLAB PGSTAT potentiostat controlled by NOVA 1.11 software. These tests, conducted at room temperature, employed a three-electrode cell configuration with Ag/AgClKCl (sat) as the reference electrode, a platinum wire as the counter electrode, and the working electrode's exposed surface measured 25 mm^2. The different areas of the weld zone, as well as the BM, were tested separately by individually masking the areas according to their microstructure and their corrosion behavior in the ASTM G110 test. For EIS measurements, the same electrolyte was used as for IGC testing. Before starting the EIS measurement, the samples were exposed to the electrolyte for 60 min (1-h exposure to the electrolyte before EIS data acquisition).

The EIS data were acquired potentiostatically at the open circuit potential (OCP) within a frequency range of 100 kHz to 5 MHz, applying a 10 mV amplitude signal and an acquisition rate of 10 points per decade.

2.6 | X-ray photoelectron spectroscopy (XPS) analysis

The chemical compositions of Al alloy surfaces with the same surface preparation as for IGC tests were analyzed by XPS using a ThermoFisher Scientific spectrometer, model K-α+. The beam was produced by a monochromatic Al K-α radiation source. The beam diameter was comprised of 400 μm, and the analysis chamber pressure was approximately 10^{-7} Pa. The binding energy scale was calibrated with respect to the carbon peak (C1s) at 284.8 eV. Survey spectra of the welded samples at the different welding zones were acquired.

3 | RESULTS

3.1 | Evaluation of the microstructure

Figure 1 shows the grain morphology of a welded sample, revealing varied shapes within the weldment. Highly refined grains characterize the SZ, while the TMAZ exhibits elongated and deformed grains. In the HAZ, the grain morphology closely resembles that of the BM, showing to be elongated. These grain modifications in the weld zones can be associated with the deformation and temperatures the BM underwent in each region, as shown in Figure 1 and the influence of tool rotation. Furthermore, the diverse impact of the thermal cycles within the weldment influences the characteristics of nano-scale intermetallic particles, affecting their morphology and distribution. In addition, the temperature profile of the AA2098-T351 alloy welded by FSW was obtained from thermal simulation, as shown in Figure 2, which presented the low-temperature and high-temperature HAZs, respectively.

In our recent study,[27] we investigated numerous nanometric phases in AA2098-T351 alloy welded by FSW, focusing on their morphology and distribution. However, the characterization of GB in the context of precipitate type and quantity, as well as the susceptibility of zones with different microstructures to IGC, was not addressed. The IGC and exfoliation in Al–Cu–Li alloys are often attributed to the galvanic coupling of nano-sized particles and the PFZ at grain boundary regions. In this study, we specifically characterized the phases

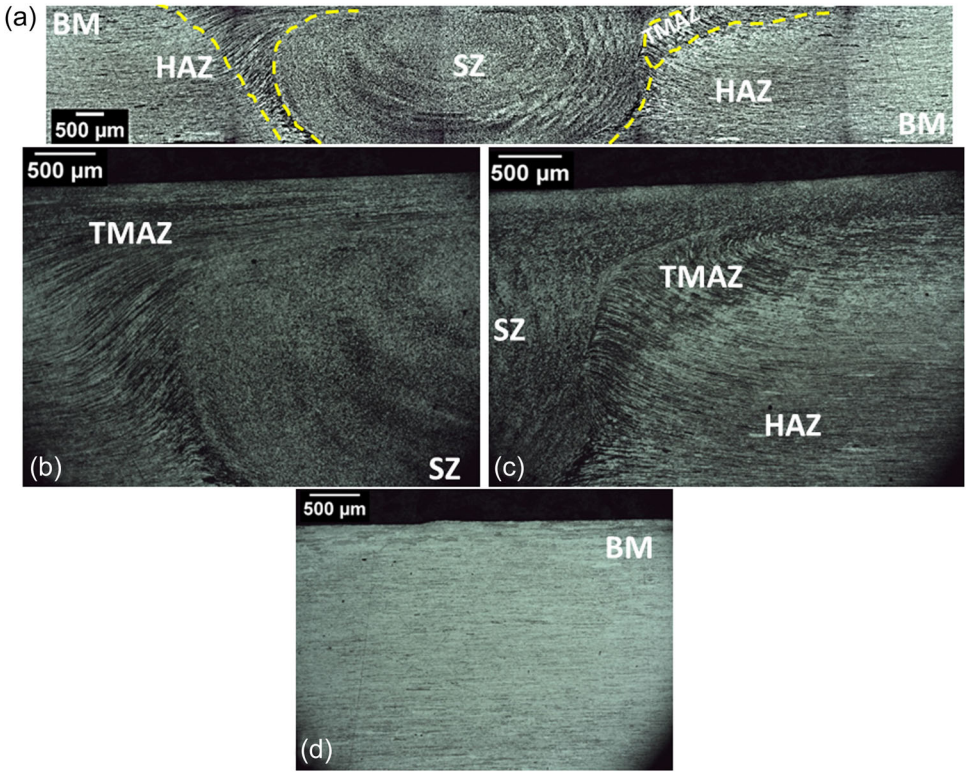

FIGURE 1 Optical micrographs of the cross section of the welded AA2098-T351 alloy showing the grain morphologies in the various zones. (a) Welding overview; (b) retreating side welding zones; (c) advancing side welding zones; and (d) base metal (BM) zone. [Color figure can be viewed at wileyonlinelibrary.com]

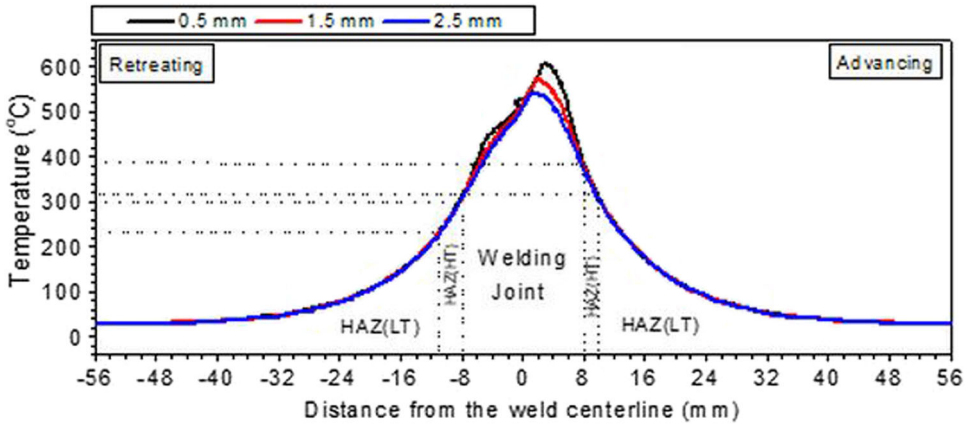

FIGURE 2 Temperature profile of the AA2098-T351 alloy welded by friction stir welding (FSW) obtained by thermal simulation.[27] The heat-affected zone (HAZ) (low temperature [LT]) and HAZ (high temperature [HT]) correspond to low-temperature heat-affected zone, low temperatures, and high-temperature heat-affected zone, respectively, and Welding Joint represents a region comprising the thermomechanically affected zone (TMAZ) and stir zone (SZ). [Color figure can be viewed at wileyonlinelibrary.com]

precipitated at the GB and their surroundings. Figure 3 depicts some of the GBs in the BM, and T1 (Al_2CuLi), β/δ ($Al_3(Zr, Li)$), and θ (Al_2Cu) phases were identified. The Ω (Al_2Cu) phase was found in proximity to the GB but not directly at the GB.

In the HAZ, only T1 and β/δ phases were identified, as shown in Figure 4. In addition, in this zone, the T1 phase exhibited a coarser, shorter structure with lower quantities compared with the BM. Moreover, PFZs were identified. The temperatures reached in the HAZ were below 300°C on the retreating side (RS) and remained under 400°C on the advancing side (AS). The welding joint (WJ), comprising the TMAZ and SZ welding zones, recorded the highest temperatures ranging from 300°C to 620°C. Specifically, in

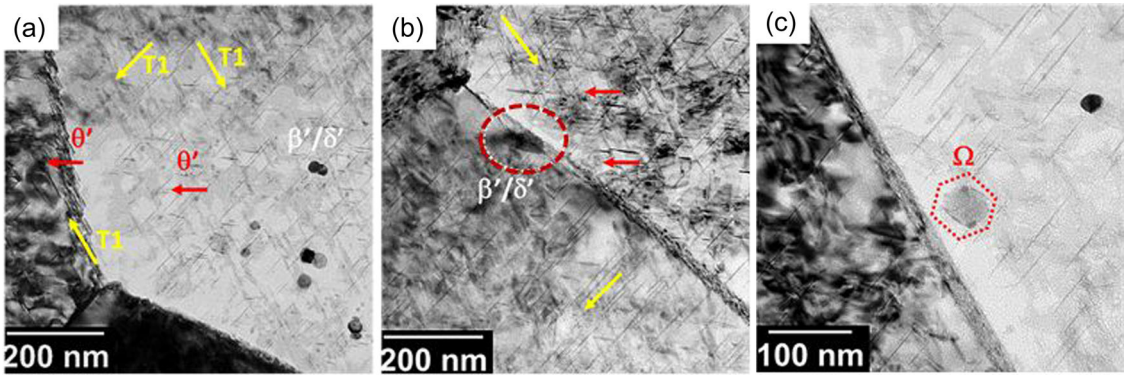

FIGURE 3 Bright field transmission electron microscopy (TEM) images of the grain boundary regions in the base metal (BM) showing the presence of nano-sized intermetallic particles in (a,b) [110] orientation and (c) [112] orientation along 111 direction. [Color figure can be viewed at wileyonlinelibrary.com]

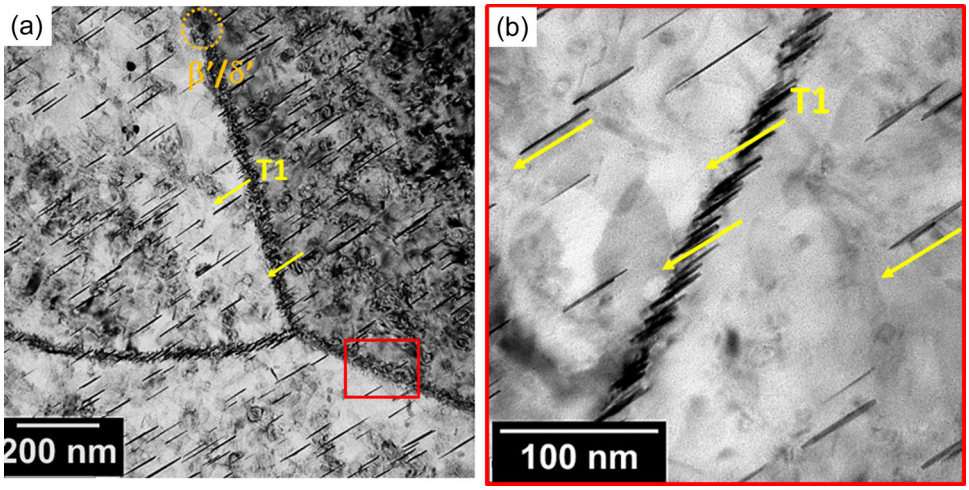

FIGURE 4 Bright field transmission electron microscopy (TEM) images (a,b) of the heat-affected zone (HAZ) showing the presence of nano-sized particles at the grain boundaries in the [112] orientation along the (200) direction. [Color figure can be viewed at wileyonlinelibrary.com]

the TMAZ corresponding to the AS, T1 was entirely absent, as shown in Figure 5a,b. In the TMAZ, β/δ phases adorned the GB, as depicted in Figure 5c. The T1 phase in the TMAZ was comparatively scarcer, smaller, and coarser than in the BM. These findings align with the temperature profile indicated in Figure 2, presenting the peak temperatures (520°C–620°C) in this specific zone. In contrast, the T1 phase was present in the SZ, although less frequently and with smaller and coarser features compared to the BM. Moreover, β/δ and Ω phases were observed at the GB of the SZ, as shown in Figure 6. A summary of the phases found at the GB of the AA2098-T351, which were welded by FSW and identified by TEM analysis, is presented in Table 1.

Figure 7 Energy dispersive X-Ray (EDX) analysis of the Al alloy particles indicates the EDX maps of the Al alloy after surface etching in preparation for the IGC test. Specifically, copper (Cu) and iron (Fe)-enriched particles were evident on the surface, with point scans unveiling the presence of a small amount of silver (Ag) over some of these particles. This observation aligns with the XPS analysis depicted in Figure 8a, which also showed the presence of Cu and Ag on the surface. Additionally, the chemical composition of several welding zones was analyzed based on peak areas, as shown in Figure 8b. Interestingly, no significant variations in the analyzed elements were observed across the scanned areas. Furthermore, one can see the points that were analyzed by XPS in Figure 8c.

3.2 | INVESTIGATION OF THE IGC RESISTANCE

After 6 h of exposure to the IGC solution, the cross-section of the tested sample was determined. The primary type of corrosion attack was intragranular, as

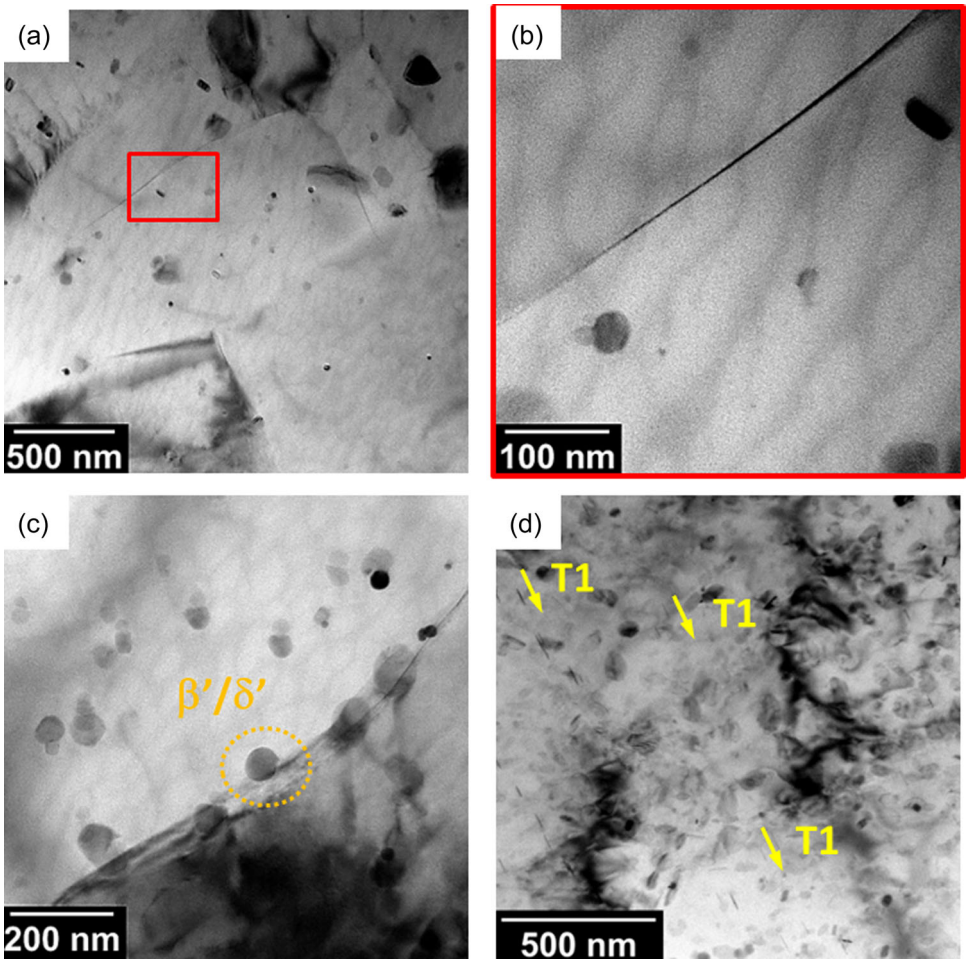

FIGURE 5 Bright field transmission electron microscopy (TEM) images of the thermomechanically affected zone (TMAZ)/heat-affected zone (HAZ) showing the presence of nano-sized particles at grain boundaries in the (a)–(b) [110] orientation and (c) [112] orientation, and (d) T1 phase in the [110] orientation. [Color figure can be viewed at wileyonlinelibrary.com]

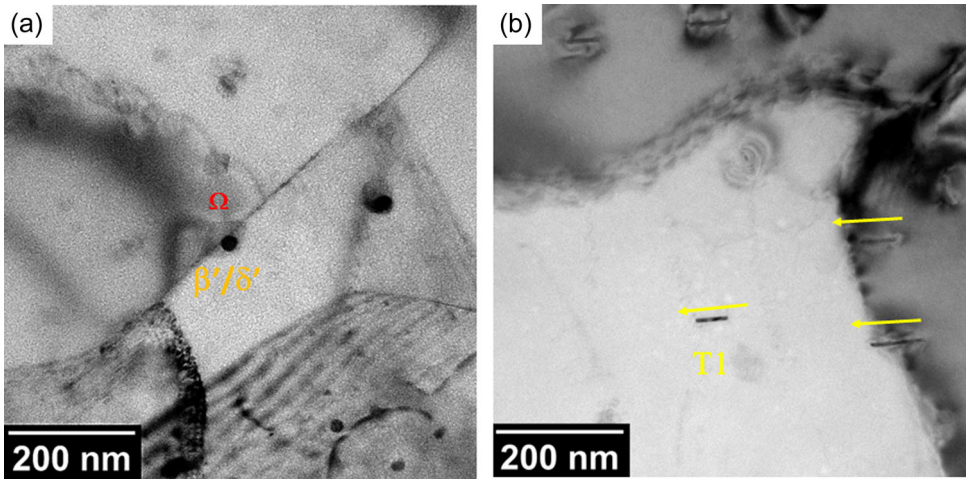

FIGURE 6 Bright field transmission electron microscopy (TEM) images of the stir zone (SZ) showing the presence of nano-sized particles at the grain boundaries: (a) Ω phase and β'/δ' in the [110] orientation; (b) T1 phase precipitation in the [110] orientation. [Color figure can be viewed at wileyonlinelibrary.com]

TABLE 1 Characteristics of the nano-sized phases located in the GB of the AA2098-T351 alloy welded by FSW.

Phase	Composition	Morphology	Location at GB
T1	Al2CuLi	lath	BM, HAZ, TMAZ, SZ
θ	Al2Cu	lath	BM
β/δ	Al3 (Zr, Li)	core/shell	BM, HAZ, TMAZ, SZ
Ω	Al2Cu	hexagonal	SZ

Abbreviations: BM, base metal; FSW, friction stir welding; GB, grain boundaries; HAZ, heat-affected zone; SZ, stir zone; TMAZ, thermomechanically affected zone.

shown in Figure 9b. The intragranular attack was featured by the complete consumption of the entire grain, as shown in Figure 9c. A second type of attack involved deeper penetration and was concentrated in the outer layers of the surface, as elucidated in Figure 9c.

In the welded AA2098-T351, the WJ exhibited heightened activity compared with the BM, evident in the formation of gas bubbles (Figure 10a,b). Cross-sectional examinations showed different corrosion susceptibilities in the HAZ, as depicted in Figure 10b, and the WJ, TMAZ, and SZ; IGC behavior is shown in Figure 10c. All welding zones presented greater susceptibility to IGC than the BM. Moreover, based on the IGC test outcomes, the HAZ could be subdivided into two regions depending on the temperatures reached during FSW: (1) the high-temperature HAZ (HAZ(HT)) exposed to higher temperatures ranging from 240°C to 300°C at the RS and from 320°C to 380°C at the AS; and (2) the low-temperature HAZ (HAZ(LT)) where temperatures remained below the specified range for HAZ (HT). Within the HAZ(HT), the predominant type of attack was IGC, as depicted in Figure 10d. On the other hand, the HAZ(LT) exhibited susceptibility to both intragranular and exfoliation corrosion, with the severity of the attack surpassing that observed in the BM. The EIS results, depicted in Figure 11, exhibit strikingly similar diagrams for all three tested zones, hinting at the presence of 3 × constants. Upon magnifying the high-frequency data, a capacitive arc with a 45° angle to the real axis is revealed. Although typically associated with diffusion-controlled processes, the appearance of this response in a high-frequency range rules out such an association, as the diffusion of chemical species in solution is known to be a slow process.

It is critical to note that the alloy's corrosion attack in the IGC solution boasts high kinetics. After a brief exposure to the environment, the alloy surface becomes notably porous, as shown in Figures 9 and 10. By de Levie,[28,29] the EIS response of a greatly attacked electrode is featured by a Warburg-like behavior. The high-frequency time constant may be associated with the response of the pit system to electrochemical reactions occurring at the conductive pit walls. In the high-frequency range, the initial capacitive loop reflects pitting corrosion on the surface. Moving to the medium-frequency time constant, the Nyquist diagrams exhibit a flattened capacitive arc, indicative of charge transfer-controlled reactions and the charging of the double layer. The low-frequency capacitive loop analysis proposes its association with corrosion processes occurring at the alloy surface. Notably, based on the EIS data, the BM exhibited the highest impedances at low frequencies, presenting its superior resistance to IGC among the zones tested. In fact, the intragranular corrosion mechanism of the 2098-T351 alloy has been reported, as explained in our previous research.[30,31] These EIS results align seamlessly with the observed surface features after the post-IGC test.

Upon comparing the analyzed zones, it was clear that the BM shows an intragranular attack and the attack is more superficial compared with the other zones tested. It is important to highlight the fact that EIS cannot be used to distinguish localized corrosion. However, the argument here is that in the IGC facilitating environment that is being used in this study, the BM exhibits the highest resistance, and this is evident in the EIS. An increase in the Bode Z modulus was noticed from the weld-affected zones (the HAZ and SZ) to the BM, as shown in Figure 11b. In the SZ, the fundamental form of corrosion was an intergranular attack, penetrating deeply into the alloy. In the HAZ, two distinct forms of attack were observed: intergranular and intragranular. In the outer layers of the surface, intragranular attack predominated, while IGC prevailed in the inner layers of the surface.

It should be noted that the BM and the HAZ have the same grain structure. Thus, the differences in the corrosion morphology observed are not due to grain structure but due to differences in preferential susceptible regions between the GB and grain interior. While the grain interiors were attacked in the BM, the preferentially attacked regions were the GB in the HAZ and SZ. Furthermore, the depth of attack was not more than 130 $\mu\mu$m in the BM but was over 200 μm in the HAZ and SZ, as well as can be compared in Figures 9 and 10.

Based on the results, the primary corrosion phenomenon in the welded AA2098-T351 exposed to the IGC standard test solution can be ascribed as follows. The significant mechanical and thermal effects in the SZ led to recrystallization and the dissolution of substantial amounts of the T1 phase, decreasing the susceptibility of this zone to intragranular attack. The elevated temperatures reached in the SZ facilitated accelerated natural aging processes, specifically along GB where solute-depleted zones are preferentially

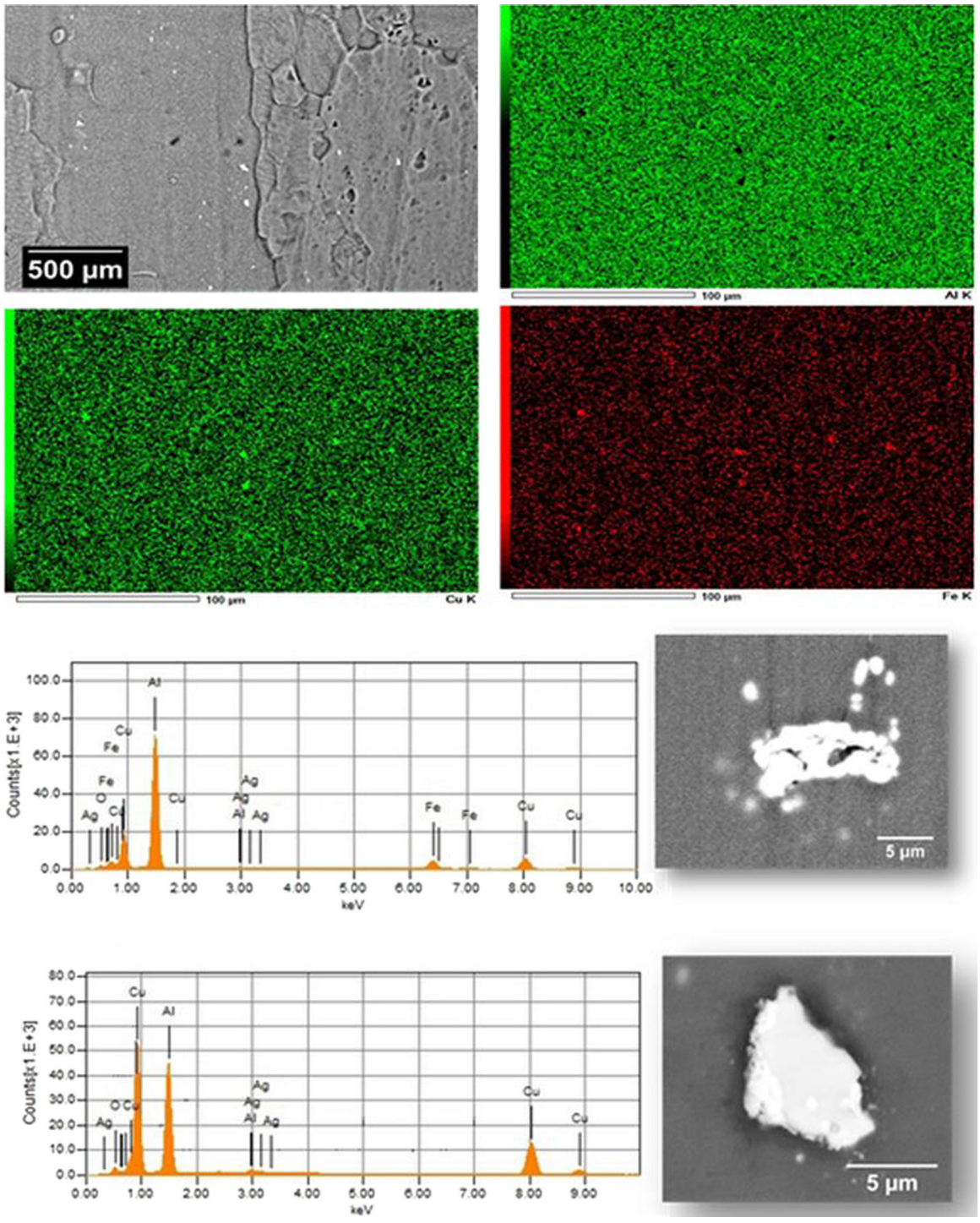

FIGURE 7 EDX maps of the AA2098-T351 surface etched in acid solution before immersion in intergranular corrosion (IGC) test solution and point analysis of typical micrometric particles present in the alloy. [Color figure can be viewed at wileyonlinelibrary.com]

located. This mechanism explains the alloy's susceptibility to intergranular attack. TEM analyses further revealed anodic phases, such as δ (Al_3Li), preferentially located at the GBs of the SZ because of the aging process.[27] Furthermore, the cathodic nature of the micrometric intermetallic particles was considered to be critical in the propagation of IGC in the SZ (Figure 12c). A galvanic coupling formed between these micrometric particles at the GB and the interior of grains, amplifying the susceptibility of this region to IGC.

High resistance to IGC was observed in the HAZ(HT) near the WJ. However, IGC was evident in the WJ, and exfoliation was also observed in the outer regions of the welded sample. This discrepancy in microstructural

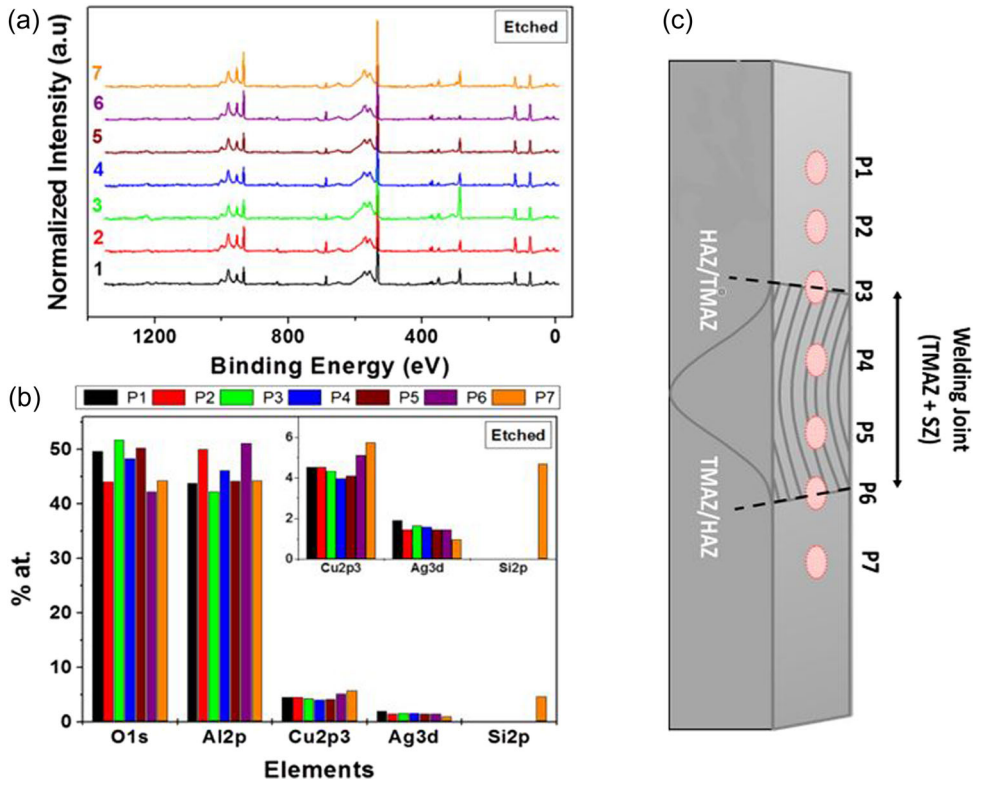

FIGURE 8 (a) Survey spectra obtained (using AlKα radiation) from different regions of the welded AA2098-T351 etched in acid solution before immersion in intergranular corrosion (IGC) solution; (b) elements atomic percentage variation according to welding zones, and (c) a schematic diagram presents the points analyzed by X-ray photoelectron spectroscopy (XPS). [Color figure can be viewed at wileyonlinelibrary.com]

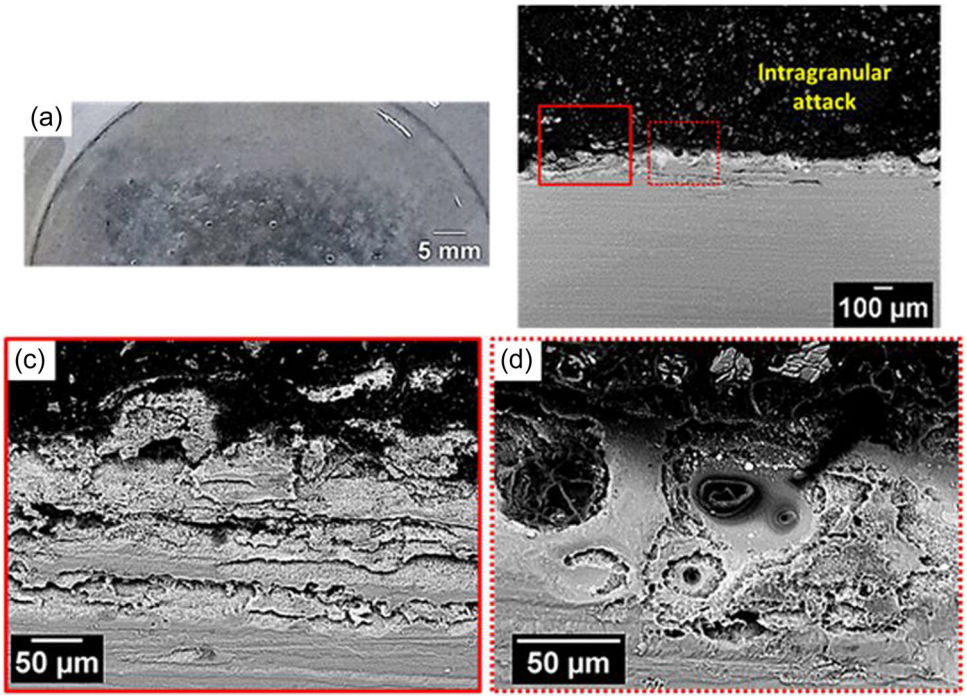

FIGURE 9 (a) In situ optical image of the base metal (BM) sample during immersion test in the intergranular corrosion (IGC) solution and (b) intragranular attack. (c–d) Cross section of AA2098-T351 after immersion in IGC test solution for 6 h showing intragranular attack in the BM. [Color figure can be viewed at wileyonlinelibrary.com]

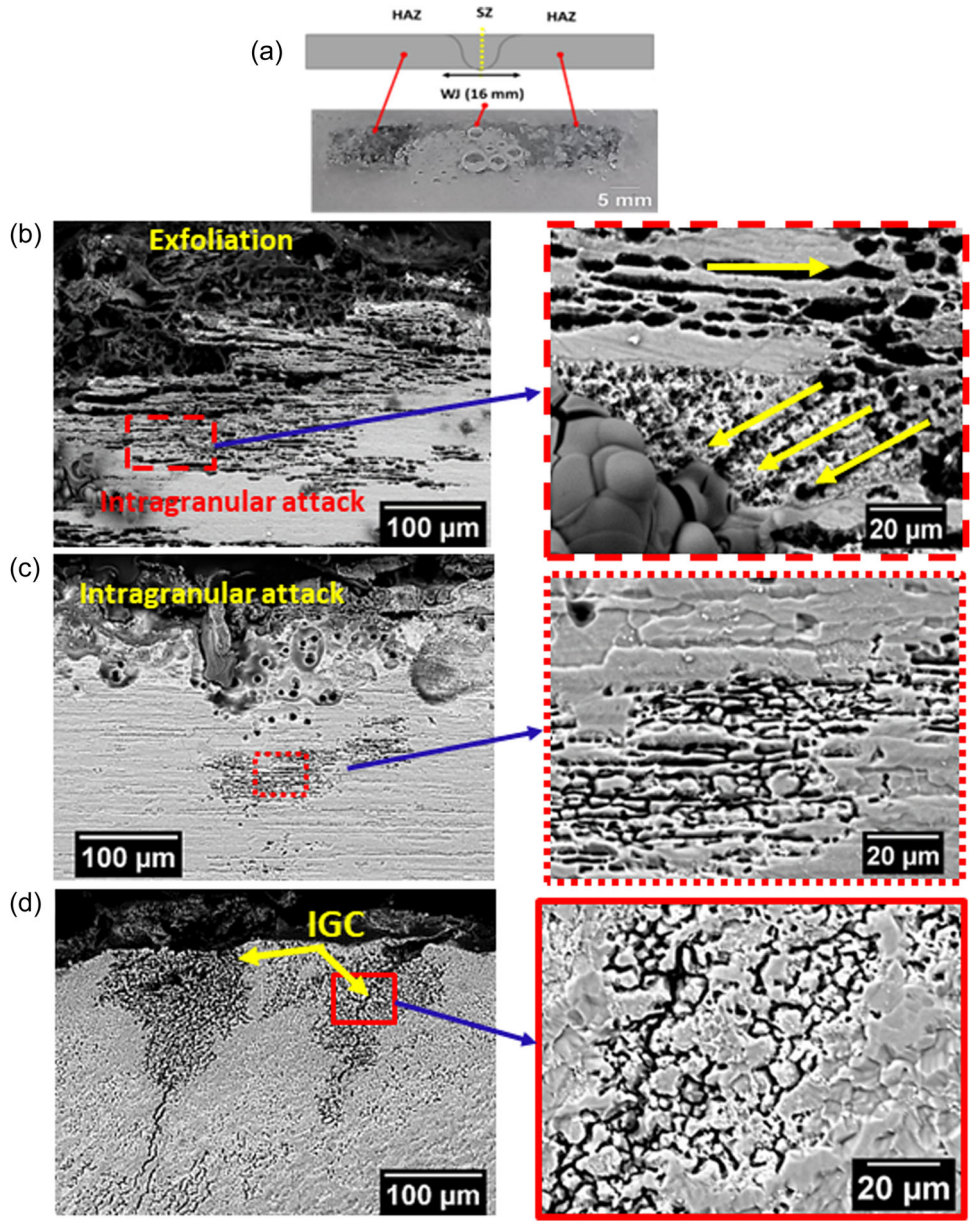

FIGURE 10 (a) In situ optical and (b–d) scanning electron microscopy (SEM) images of the welded AA2098-T351 during and after exposure for 6 h to intergranular corrosion (IGC) solution. (a) Welded sample during exposure to the IGC test solution. (b–d) Cross-sectional views of (b) heat-affected zone (HAZ)(low temperature [LT]); (c) HAZ(high temperature [HT]); and (d) welding joint (stir zone [SZ] and thermomechanically affected zone [TMAZ]). [Color figure can be viewed at wileyonlinelibrary.com]

characteristics between the outer and inner layers is associated with differences in cooling rates across the surfaces of the plate. Lower cooling rates in the interior of the plate fostered grain boundary segregation. The presence of micrometric particles at the GBs in these regions increases their susceptibility to IGC compared with the outer layers.

The observation of IGC, as depicted in Figure 12b, can be explained by the presence of coarse T1 phase at the sub-GB in the HAZ(LT), promoting exfoliation in this region despite the low content of the T1 phase. The smaller and coarser T1 phase, coupled with broad PFZs in this zone, leads to a high potential difference between the anodic sites at the GB and the PFZ. As a consequence, this promoted high electrochemical activity in this region. The similarity in the corrosion mechanism between the BM and HAZ(LT), presented by the absence of an IGC attack, is evidence that the low temperatures in the HAZ(LT) had no potential influence on the alloy microstructure, as shown in Figure 12c.

Overall, the diverse thermal cycles encountered in distinct regions during the FSW process created a notable

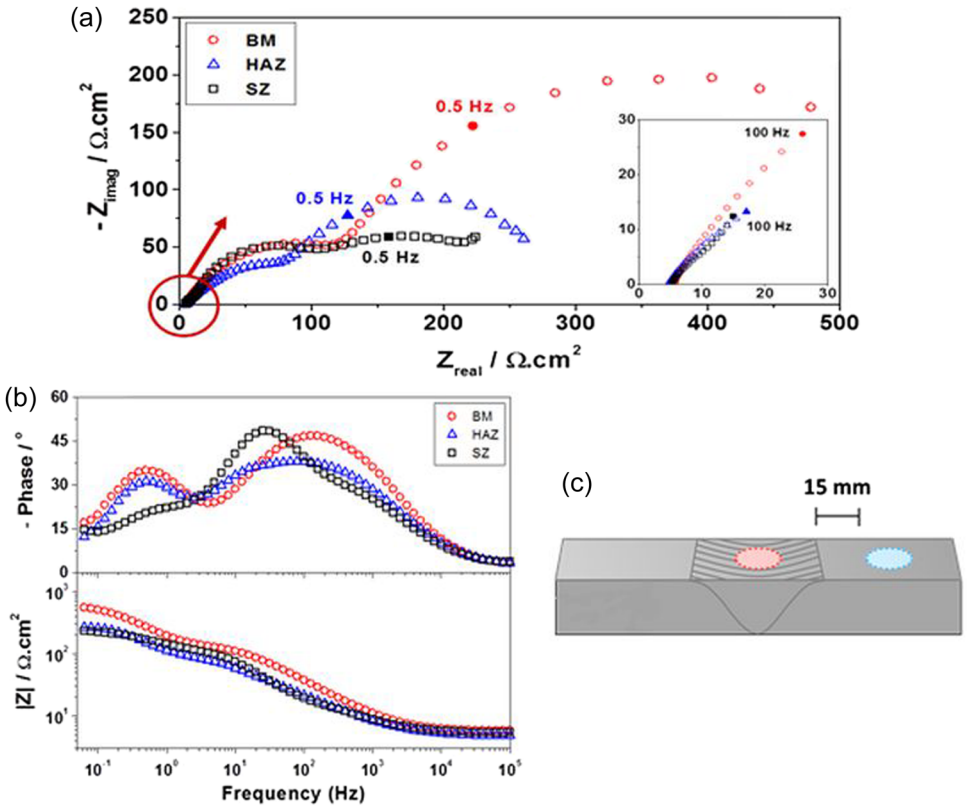

FIGURE 11 Electrochemical impedance measurements (EIS) diagrams of the different zones of the AA2098-T351 welded by friction stir welding (FSW) after 1 h of immersion in intergranular corrosion (IGC) test solution. (a) Nyquist diagrams; (b) Bode phase angle and Z modulus diagrams; and (c) illustration of the areas analyzed by EIS. [Color figure can be viewed at wileyonlinelibrary.com]

impact on the susceptibility of the AA2028-T351 Al alloy to corrosion. Table 2 underscores the altered corrosion mechanisms observed in the analyzed zones.

4 | DISCUSSION

The study of IGC susceptibility in AA2098-T351 FSW provides detailed insights into the intricate dynamics between the welding process, microstructure, and corrosion behavior of the alloy. Utilizing EIS and ASTM G110-92 practice, this study delves into distinct welding zones in comparison with the pristine BM. The microstructural changes induced by FSW are explained by TEM analysis, revealing a robust correlation between these changes and the IGC susceptibility observed in diverse zones.

The results of this study underscore the importance of the FSW process on the propagation of attack and the susceptibility to IGC in the AA2098-T351 alloy. Despite the common corrosion phenomenon identified through EIS, the mode of attack propagation varied across different welding zones. The BM indicated susceptibility to intragranular attack, whereas the WJ region (i.e., TMAZ and SZ) displayed higher susceptibility to IGC. The higher susceptibility of IGC correlated with the reduced T1 phase content, associated with larger PFZs around GBs, the anodic nature of GB, and the grain shape in this specific region. It is noteworthy that IGC susceptibility standard practice emerged as a valuable technique for comparing the corrosion behavior of distinct welding zones, making it easy to correlate both visual corrosion characteristics and electrochemical responses.

Overall, the validation by ASTM G110-92 and of the EIS findings highlight the electrochemical foundations of the observed corrosion features. The intertwined influences of temperature, microstructure, and corrosion susceptibility seem to intricately contribute to the heightened corrosion resistance observed in HAZ(HT) as evidenced by both methodologies. As a result, this study contributes to showing how the temperature variations during welding induce microstructural alterations, and the consequent corrosion susceptibility of the AA2098-T351 alloy, showing the importance of the welding optimizing studies to increase the performance and longevity of AA2098-T351 alloys in practical applications.

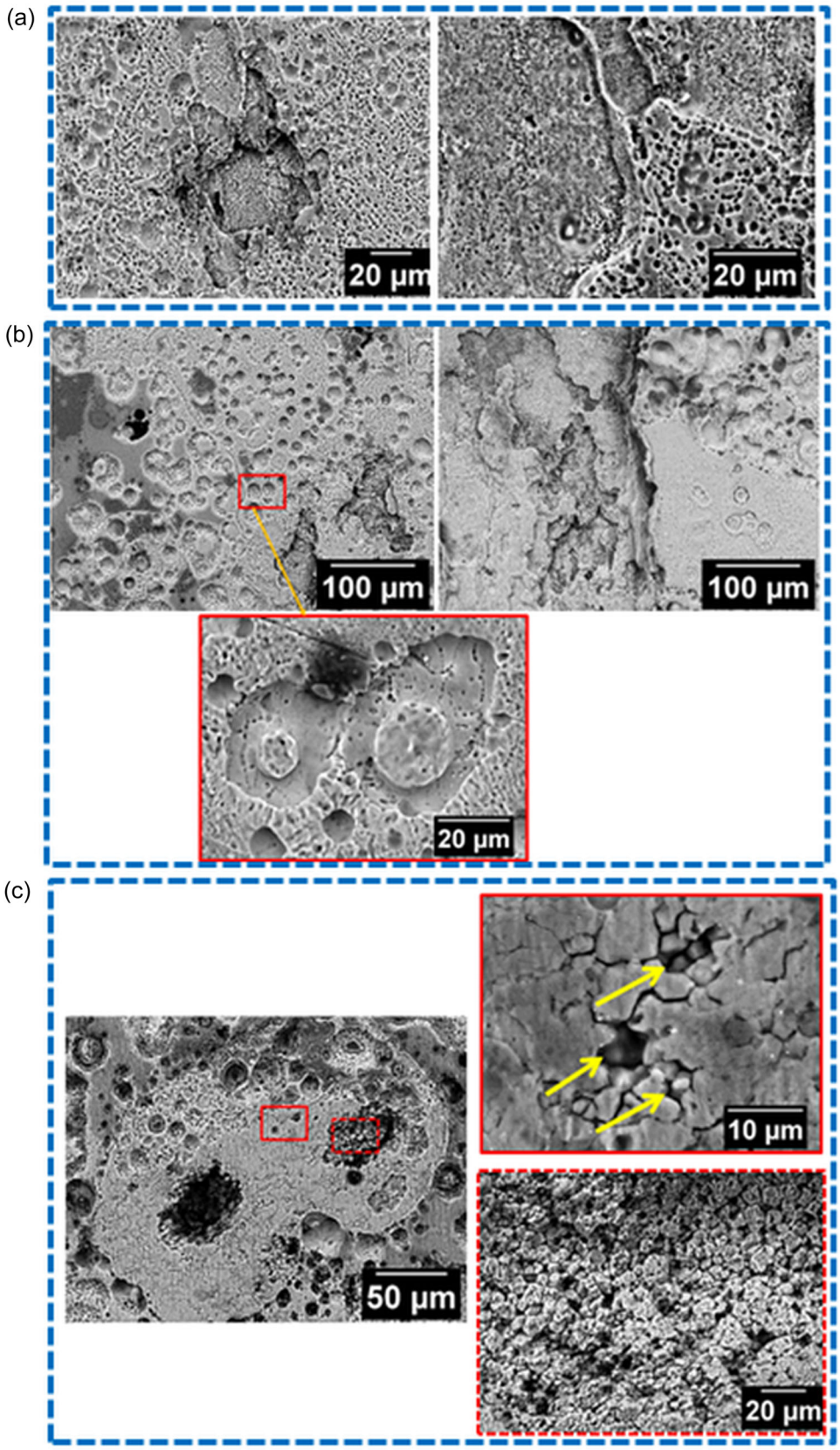

FIGURE 12 Scanning electron microscopy (SEM) images of the different zones of the AA2098-T351 welded by friction stir welding (FSW) exposed to intergranular corrosion (IGC) standard test solution for 1 h after electrochemical impedance measurements (EIS) test. (a) base metal (BM); (b) heat-affected zone (HAZ); and (c) stir zone (SZ). [Color figure can be viewed at wileyonlinelibrary.com]

TABLE 2 Corrosion mechanisms at different zones of the AA2098-T351 welded by FSW exposed to IGC test solution.

Welding Zone	Main corrosion features
Welding joint (TMAZ+SZ)	IGC
HAZ (HT)	Pitting, IGC, intragranular attack
HAZ (LT)	Intragranular attack
BM	Intragranular attack

Abbreviations: BM, base metal; FSW, friction stir welding; HAZ, heat-affected zone; IGC, intergranular corrosion; TMAZ, thermomechanically affected zone.

5 | CONCLUSION

The susceptibility of AA2098-T351, welded by the FSW process, was evaluated using ASTM G110-92 practice and EIS, accompanied by TEM and SEM analyses of the microstructure of the alloy. The study unveiled remarkable microstructural alterations induced by FSW, affecting IGC susceptibility in several zones compared with the BM. In the HAZ, low temperatures caused partial dissolution and coarsening of nano-sized particles, increasing corrosion susceptibility. In contrast, high temperatures in the SZ promoted T1 phase dissolution and its segregation at GB, enhancing IGC susceptibility. The BM exhibited intragranular attack with high activity in the IGC test solution. ASTM G110-92 successfully differentiated the HAZ into high-temperature (HAZ(HT)) and low-temperature (HAZ(LT)) zones, with the HAZ(HT) showing superior corrosion resistance. EIS results aligned with the ASTM G110-92, reinforcing the correlation between microstructural changes and IGC susceptibility in FSW-welded AA2098-T351 alloy.

ACKNOWLEDGMENTS

Acknowledgments are due to Dr. Maysa Terada, Victor Ferrinho Pereira, and Rafael Giorgão from Brazilian Nanotechnology National Laboratory (LNNano) for the welding of AA2098-T351 plate. Acknowledgments are also due to, Dr. Antonello Astarita from University of Naples "Federico II", Italy Dept. of Chemical, Materials and Industrial Production Engineering for providing the test material. Thanks are also due to Dr. Izabel Fernanda Machado and Raphael Oliveira Ferreira from the University of São Paulo, Dept. of Mecatronic and Mechanical Sistems for the SEM facilities. This study was funded by CAPES (Capes/Cofecub No 806-14), FAPESP:2013/13235-6, CAPES: 99999.000332/2016-00 and 99999.000400/2016-05; FAPES:Proc.2017/03095-3 and Proc. 2018/06880-6.

CONFLICT OF INTEREST STATEMENT

The authors declare no conflict of interest.

DATA AVAILABILITY STATEMENT

Data that support the findings of this study are available on request from the corresponding author.

ORCID

Mariana X. Milagre http://orcid.org/0000-0003-2048-2863
Uyime Donatus http://orcid.org/0000-0001-8871-3571
Caruline S. C. Machado http://orcid.org/0000-0003-4172-119X
Renato A. Antunes http://orcid.org/0000-0003-1540-6495
Sajid Farooq http://orcid.org/0000-0001-9914-5987

REFERENCES

[1] J. C. Kelly, J. L. Sullivan, A. Burnham, A. Elgowainy, *Environ. Sci. Technol.* **2015**, *49*, 12535.
[2] J. Rissman, C. Bataille, E. Masanet, N. Aden, W. R. Morrow III, N. Zhou, N. Elliott, R. Dell, N. Heeren, B. Huckestein, J. Cresko, S. A. Miller, J. Roy, P. Fennell, B. Cremmins, T. Blank, D. Hone, E. Williams, S. la, R. Can, B. Sisson, M. Williams, J. Katzenberger, D. Burtraw, G. Sethi, H. Ping, D. Danielson, H. Lu, T. Lorber, J. Dinkel, J. Helseth, et al., *Appl. Energy* **2020**, *266*, 114848.
[3] T. Dursun, C. Soutis, *Mater. Design* **2014**, *56*, 862.
[4] P. Threadgill, A. Leonard, H. Shercliff, P. Withers, *Int. Mater. Rev.* **2009**, *54*, 49.
[5] G. Çam, V. Javaheri, A. Heidarzadeh, *J. Adhes. Sci. Technol.* **2023**, *37*, 162.
[6] D. Prabhakar, A. Korgal, A. K. Shettigar, M. A. Herbert, M. P. G. Chandrashekharappa, D. Y. Pimenov, K. Giasin, *J. Manuf. Mater. Process.* **2023**, *7*, 181.
[7] W. Zhang, Y. Mao, P. Yang, N. Li, L. Ke, Y. Chen, *Materials* **2022**, *15*, 969.
[8] L. Shi, X. Dai, C. Tian, C. Wu, *Mater. Sci. Eng. A* **2022**, *858*, 144169.
[9] P. Chen, T. Li, X. Yin, Y. Tang, G. Liu, S. Wang, B. Huang, Z. zhang. *J. Mater. Res. Technol.* **2023**, *24*, 1991.
[10] N. Li, Y. Xu, W. Li, P. Niu, A. Vairis, *Weld. World* **2022**, *66*, 951.
[11] C. Gao, Z. Zhu, J. Han, H. Li, *Mater. Sci. Eng. A* **2015**, *639*, 489.
[12] A. Shukla, W. Baeslack Iii, *Scr. Mater.* **2007**, *56*, 513.
[13] N. Nayan, M. Yadava, R. Sarkar, S. N. Murty, N. Gurao, S. Mahesh, M. Prasad, I. Samajdar, *Mater. Charact.* **2020**, *159*, 110002.
[14] Y. Pan, D. Zhang, H. Liu, L. Zhuang, J. Zhang, *J. Alloys Compd.* **2021**, *853*, 157199.
[15] Y. Yang, J. Bi, H. Liu, Y. Li, M. Li, S. Ao, Z. Luo, *J. Manuf. Process.* **2022**, *82*, 230.
[16] J. Kertz, P. Gouma, R. Buchheit, *Metall. Mater. Trans. A* **2001**, *32*, 2561.
[17] C. Luo, S. P. Albu, X. Zhou, Z. Sun, X. Zhang, Z. Tang, G. E. Thompson, *J. Alloys Compd.* **2016**, *658*, 61.
[18] J. V. d.S. Araujo, R. M. P. d. Silva, U. Donatus, C. d.S. C. Machado, I. Costa, *Mater. Res.* **2020**, *23*, 1.

[19] P. Rambabu, N. Eswara Prasad, V. Kutumbarao, R. Wanhill, *Aerospace Materials and Material Technologies: Volume 1: Aerospace Materials* Springer **2017**, pp. 29–52.
[20] X. Wang, G. Li, Q. He, J. Jiang, D. Li, W. Shao, L. Zhen, *Corros. Sci.* **2023**, *211*, 110845.
[21] J. Chen, K. Ling, P. Deng, W. Mo, C. Tang, Z. Ouyang, B. Luo, Z. Bai, *Mater. Today Commun.* **2023**, *34*, 105363.
[22] W. LIANG, P. Qinglin, H. Yunbin, L. Yunchun, Z. Yingchun, L. Congge, *Rare Metals* **2008**, *27*, 146.
[23] R. Ambat, E. Dwarakadasa, *Corros. Sci.* **1992**, *33*, 681.
[24] C. Kumai, J. Kusinski, G. Thomas, T. Devine, *Corrosion* **1989**, *45*, 294.
[25] M. Chen, R. Hwang, C. Chou, *Sci. Technol. Weld. Join.* **1999**, *4*, 21.
[26] V. Proton, J. Alexis, E. Andrieu, J. Delfosse, M.-C. Lafont, C. Blanc, *Corros. Sci.* **2013**, *73*, 130.
[27] M. X. Milagre, N. V. Mogili, U. Donatus, R. A. Giorjão, M. Terada, J. V. S. Araujo, C. S. Machado, I. Costa, *Mater. Charact.* **2018**, *140*, 233.
[28] R. De Levie, *Electrochim. Acta* **1963**, *8*, 751.
[29] R. De Levie, *Electrochim. Acta* **1964**, *9*, 1231.
[30] M. X. Milagre, U. Donatus, C. S. Machado, J. V. S. Araujo, R. O. Ferreira, R. M. P. Silva, R. A. Antunes, I. Costa, *J. Mater. Res. Technol.* **2019**, *8*, 5916.
[31] M. X. Milagre, U. Donatus, C. S. Machado, J. V. S. Araujo, R. M. P. da Silva, B. V. G. de Viveiros, A. Astarita, I. Costa, *Corros. Eng. Sci. Technol.* **2019**, *54*, 402.

How to cite this article: M. X. Milagre, U. Donatus, N. V. Mogili, C. S. C. Machado, J. V. S. Araujo, R. M. P. Silva, R. A. Antunes, S. Farooq, I. Costa, *Mater. Corros.* **2024**, *75*, 1359–1372. https://doi.org/10.1002/maco.202314245